

Rayleigh–Taylor instabilities with anisotropic lithospheric viscosity

Einat Lev and Bradford H. Hager

Department of Earth, Atmospheric and Planetary Science, Massachusetts Institute of Technology, Cambridge, MA, USA. E-mail: einatlev@MIT.EDU

Accepted 2008 January 9. Received 2007 October 18; in original form 2007 April 9

SUMMARY

Rocks often develop fabric when subject to deformation, and this fabric causes anisotropy of physical properties such as viscosity and seismic velocities. We employ 2-D analytical solutions and numerical flow models to investigate the effect of anisotropic viscosity (AV) on the development of Rayleigh–Taylor instabilities, a process strongly connected to lithospheric instabilities. Our results demonstrate a dramatic effect of AV on the development of instabilities—their timing, location, and, most notably, their wavelength are strongly affected by the initial fabric. Specifically, we find a significant increase in the wavelength of instability in the presence of AV which favours horizontal shear. We also find that an interplay between regions with different initial fabric gives rise to striking irregularities in the downwellings. Our study shows that for investigations of lithospheric instabilities, and likely of other mantle processes, the approximation of isotropic viscosity may not be adequate, and that AV should be included.

Key words: Creep and deformation; Seismic anisotropy; Dynamics of lithosphere and mantle; Rheology: crust and lithosphere; Rheology: mantle.

1 INTRODUCTION

The response of anisotropic materials to stress depends on the orientation of the stress relative to the orientation of the anisotropy. Anisotropy of seismic wave speed in rocks has been studied vigorously in the last decades, both in experimental (e.g. Zhang & Karato 1995) and theoretical work (e.g. Kaminski & Ribe 2001). It has been shown that the deformation of rocks and minerals leads to development of crystallographic preferred orientation (CPO), which leads to seismic anisotropy (Karato *et al.* 1998). In addition, rotation of grains and inclusions, alignment of microcracks or melt lenses, and layering of different phases all lead to the development of shape preferred orientation (SPO), an important source for seismic anisotropy (e.g. Crampin 1978; Holtzman *et al.* 2003; Maupin *et al.* 2005).

The anisotropic viscosity (AV) of earth materials has received less attention, but its effects are dramatic. Using laboratory experiments, Durham & Goetze (1977) showed that the strain rate of creeping olivine with pre-existing fabric depends on the orientation of the sample and can vary by up to a factor of 50. This is because the orientation of the sample relative to the applied stress determines which slip systems are activated. In the experiments of Bai & Kohlstedt (1992) on high-temperature creep of olivine and those of Wendt *et al.* (1998) on peridotites, the measured strain rate depended strongly on the relative orientation of the applied stress to the sample crystallographic axis. Honda (1986) calculated the long-wavelength constitutive relations for a transversely isotropic material, and concluded that these can be characterized by two viscosities—a normal viscosity (η_N), associated with principal stresses normal to the easy-shear planes, and a shear viscosity (η_S), associated with shearing parallel to the easy-shear planes. More theoretical work (e.g.

Weijermars 1992; Mandal *et al.* 2000; Treagus 2003) was done to assess the AV of composite materials, depending on the geometry and the relative strength of each component. These studies imply that regions of the earth that are not likely to become anisotropic by means of dislocation creep and LPO development may exhibit AV due to the deformation of composite materials, such as most natural rocks, and two-phase materials, such as partially molten rocks. Recently, Pouilloux *et al.* (2007) discussed the anisotropic rheology of cubic materials and the consequences for geological materials.

A few geodynamic studies have examined the effect of AV on mantle flow. Richter & Daly (1978) and Saito & Abe (1984) used analytical solution methods to investigate the development of Rayleigh–Bénard instabilities in a viscously anisotropic medium with specified easy-shear geometry, and found a connection between the anisotropy of the fluid and the length-scales of the convection cells. In a very instructive study a few years later, Christensen (1987) showed that the inclusion of AV affects two important mantle flows—postglacial rebound and thermal convection. For example, Christensen (1987) pointed out a spatial offset between mass anomalies and the resulting geoid signal in the presence of AV, which may help to reconcile the argued mismatch between observed uplift history near ice sheet margins and models of strong viscosity stratification in the mantle. AV also leads to channelling of flow into low viscosity region such as hot rising plumes. Nonetheless, Christensen concluded that the actual effect of AV in the earth's mantle would be much smaller, as the fabric required for creating AV would be obliterated by the highly time-dependent flow. However, the abundant evidence for seismic anisotropy in the earth and its strong correlation with tectonic processes and features suggest that large parts of the mantle maintain fabric for long times. Pre-existing mechanical

anisotropy in the lithosphere was shown to have an effect in various tectonic settings such as oceanic shear zones (Michibayashi & Mainprice 2004) and continental break-up parallel to ancient orogens (Vauchez *et al.* 1998).

Recently, Moresi *et al.* (2002, 2003) presented an efficient algorithm for including an AV that evolves with the flow in geodynamic models. They demonstrated the new algorithm in a series of papers, looking at various geological problems, including folding of a layered medium and thermal convection. We employ this technique here to investigate lithospheric instabilities in the presence of AV.

The lithosphere is often identified as the cold upper thermal boundary layer of Earth's convecting mantle. The colder temperature of the lithosphere makes it more dense than the asthenosphere underneath, and leads to an unstable density layering (Houseman *et al.* 1981). This density instability may be further enhanced by thickening of the lithosphere due to convergence (Molnar *et al.* 1998) or emplacement of dense material (eclogite) at the base of the lithosphere (Elkins-Tanton & Hager 2000). Lithospheric instabilities and removal of the lower lithosphere have been invoked to explain observations in the New England Appalachians (Robinson 1993), the Canadian Appalachians (Murphy *et al.* 1999), Europe (Wenzel *et al.* 1997), Argentina (Kay *et al.* 1994), the North China craton (Fan *et al.* 2000; Wu *et al.* 2005) and Tibet (England & Houseman 1989). Regions of high seismic velocity underneath southern California (Humphreys & Clayton 1990; Kohler 1999; Yang & Forsyth 2006) are also interpreted as cold material sinking from the bottom of the lithosphere, probably as part of 3-D small-scale convection in the region (Humphreys & Hager 1990) or Rayleigh–Taylor instabilities (Billen & Houseman 2004). Upwelling of hot asthenospheric material following removal of the lower lithosphere has been suggested to explain, for instance, the massive flood basalts in Siberia (Elkins-Tanton & Hager 2000).

The removal of the bottom of the lithosphere due to a density instability can be approximated as a Rayleigh–Taylor instability (Conrad & Molnar 1997). Previous studies of Rayleigh–Taylor instabilities addressed the effect of the density structure, the wavelength of the density perturbation between the layers, and the rheology of the layers, on the timing and location of instability onset (e.g. Whitehead 1986; Houseman & Molnar 1997; Conrad & Molnar 1999; Billen & Houseman 2004). Here we demonstrate the significance of pre-existing and evolving fabric.

2 ANISOTROPIC VISCOSITY AND THE WAVELENGTH OF INSTABILITIES

We begin our investigation with a simple conceptual setup: a dense anisotropic layer laying over a more buoyant isotropic half-space. All of the models in this study are 2-D. The interface between the two layers is perturbed by a small initial displacement $w(x) = w_0 \cos(kx)$, where x is the horizontal direction, and k is the wavenumber of the interface perturbation. Our goal in this section is to examine the dependence of the growth rate of instabilities on the wavenumber of the perturbation, the initial orientation—horizontal or dipping—of the easy-shear planes, and the ratio between the shear and normal viscosities. We use both an analytical solution and numerical experiments for this purpose.

2.1 Governing equations

We treat the mantle as an incompressible fluid, an approximation valid for slow viscous deformation in the upper mantle (e.g. Schubert

et al. 2001). The main equation to be solved is conservation of momentum:

$$\frac{\partial \sigma_{ij}}{\partial x_j} - \frac{\partial p}{\partial x_i} + f_i = 0, \quad (1)$$

where σ_{ij} is the deviatoric stress tensor, p is the pressure, f_i is the force acting in the i th direction, and inertia is neglected. For our case, $f_z = \rho g \hat{z}$, where z is the vertical coordinate.

The flow also has to fulfil the continuity requirement for an incompressible material:

$$\frac{\partial v_i}{\partial x_i} = 0, \quad (2)$$

where \mathbf{v} is the velocity.

A central equation for any flow model is the constitutive law, relating stress and strain in the system. The constitutive law we use in this study reflects the anisotropic rheology of the materials. The simplest form of anisotropy is transverse isotropy (TI), as for a deck of cards. As shown by Honda (1986), a TI material can be characterized by two viscosities—a normal viscosity, η_N , and a shear viscosity, η_S . This form of anisotropy can describe both a layered medium, consisting of layers of different strength, or the CPO of anisotropic minerals with a dominant easy glide plane. The normal viscosity governs deformation when the two principle stresses are oriented normal and parallel to the glide plane, while the shear viscosity governs deformation when the principle stresses are oriented at 45° to the glide plane. The exact expressions we use for our analysis are given in eqs (4) and (A1).

We note that in this formulation, materials with horizontal and vertical easy-shear directions are mathematically equivalent. This is similar to a stack of books on a shelf—it is easy to shear the stack horizontally both when the books stand up (vertical easy-shear planes) and when they lay on top each other (horizontal easy-shear planes). We thus examine two end-member setups—in one the anisotropic dense layer initially has a horizontal easy-shear direction, and in the other the easy shear direction initially dips at 45° .

2.2 Analytical solution

In this analysis we use the propagator matrix technique (e.g. Hager & O'Connell 1981) to calculate the growth rate of the instabilities as a function of the wavelength of a small perturbation in the interface between the two materials. The mean depth of the interface is at $z = 0$. The boundary conditions for our problem are no-slip at the top boundary ($z = 1$), which we take to be the base of the rigid part of the lithosphere, and vanishing of the velocities and stresses as $z \rightarrow -\infty$. By calculating the vertical velocity $v(z = 0)$ we are able to track the change in position of the boundary. The derivation is outlined in Appendix A, and an important outcome of it is that

$$v(z = 0) \equiv \frac{\partial w}{\partial t} \propto w. \quad (3)$$

Because the velocity of the interface is proportional to the amplitude of the boundary topography (eq. 3), the change in the interface depth follows an exponential growth rule: $w(z, t) = e^{\frac{t}{\tau}}$. τ , the growth rate, is a function of the wavenumber k of the perturbation w , and of the two viscosities η_N and η_S .

The results we present in Section 2.4, as well as Appendix A, give insight into the relationship between the growth rate and a range of viscosities and wavenumbers. We note here that this analysis is valid only for small interface perturbations, so we can assume that the orientation of the AV does not evolve.

2.3 Numerical experiments

To follow the instability to finite amplitude requires a numerical approach. We solve the flow equations using a finite element formulation on an Eulerian mesh embedded with Lagrangian integration-points ('particles'), as described by Moresi *et al.* (2003). In this method, particles carry the material properties, and foremost their deformation history and the derived AV. Variables such as velocity and pressure are calculated at the location of the mesh nodes, which are fixed in space. We use the software package Underworld to solve the flow equations.

2.3.1 Including anisotropy in the flow equations

To include AV in our numerical experiments, we use the particle-in-cell formulation (Moresi *et al.* 2003). By this method, the anisotropy is represented by a set of 'directors' advected through the model, analogous to particles (Mühlhaus *et al.* 2002). The directors are vector-particles pointing normal to the easy-glide plane or layer, thus defining the directions associated with η_N and η_S . In each time step of the calculation, the directors are advected and rotated by the flow, and in return determine the viscosity structure for the next time step (Mühlhaus *et al.* 2004).

The AV enters the equation of momentum through a 'correction' term added to the isotropic part of the constitutive equation relating stress and strain rate (Mühlhaus *et al.* 2002):

$$\sigma_{ij} = -p\delta_{ij} + 2\eta_N\dot{\epsilon}_{ij} - 2(\eta_N - \eta_S)\Lambda_{ijkl}\dot{\epsilon}_{kl}, \quad (4)$$

where η_N, η_S are the normal and shear viscosities, respectively, σ is the deviatoric stress tensor, and $\dot{\epsilon}$ is the strain rate tensor. Λ reflects the orientation of the directors in space, denoted by \mathbf{n} :

$$\Lambda_{ijkl} = \frac{1}{2}(n_i n_k \delta_{lj} + n_j n_k \delta_{il} + n_i n_l \delta_{kj} + n_j n_l \delta_{ik}) - 2n_i n_j n_k n_l. \quad (5)$$

The evolution of the orientation of directors in time is controlled by integration over time of

$$\dot{n}_i = -\frac{\partial v_i}{\partial x_j} n_j \quad (6)$$

(Belytschko *et al.* 2001). A more detailed description of how the anisotropy described by the directors enters the equations of flow and how it is represented in the finite element formulation is given by Mühlhaus *et al.* (2002).

2.3.2 Model setup

We carried out a suite of 2-D numerical experiments to investigate the development of instabilities in the presence of AV. The numerical models we use in this section consist of a dense layer with a uniform fabric throughout its width, overlying a more buoyant layer. The model domain is a rectangular box with an aspect ratio of 1:6.4, comprised of 240×32 elements. We place a dense layer in the top 15 per cent of the box. Because the thickness of the lower layer is much greater than that of the upper layer, our analytical solution for a layer overlying a half-space should provide a reasonable approximation to the finite-depth domain. The interface between the layers is a cosine curve with an initial amplitude of 0.01. We compare the growth rate for models with an either horizontal or dipping initial easy-shear direction for a range of interface perturbation wavelengths. We measure the non-dimensional time that it takes to displace the interface by one element length, and define this time as

the reciprocal of the growth rate. The ratio of the shear viscosity to the normal viscosity for the anisotropic material is 0.1 in all cases, in accordance with the theoretical estimations of Mandal *et al.* (2000) and Treagus (2003) and within the range of values measured in the experiments of Durham & Goetze (1977). The isotropic viscosity of the buoyant lower layer is equal to the normal viscosity (η_N) of the dense layer.

2.4 Results—a homogeneous but anisotropic upper layer

Both our numerical experiments and our analytical solution predict that the most unstable wavelength for a dense layer with a horizontal fabric is much longer than that for an isotropic layer or for a layer with a dipping fabric. From our analytical solution, we calculate the normalized values of τ for a range of wavenumbers and viscosity ratios, for both a horizontal fabric and a dipping fabric. The results are plotted in Fig. 1. For comparison, we also plot the growth-rate curves for models with an isotropic dense layer with a viscosity that equals the geometric and the arithmetic averages of the shear and normal viscosities of the anisotropic material. Fig. 1 clearly shows that the effect of anisotropy is dramatic, especially for a material with initially horizontal easy-shear direction. For such a fabric, the minimum point of the growth rate curve, which determines the most unstable wavelength, shifts to a longer wavelength as the viscosity ratio becomes smaller (blue curves in Fig. 1). For a case of a shear viscosity that is 10 times smaller than the normal viscosity, a fairly conservative estimate, the most unstable wavelength is twice as long as for the isotropic one; For $\eta_S/\eta_N = 0.01$, the increase is by a factor of 3.5. This increase in the most unstable wavelength is comparable to the effect of having an isotropic dense layer with a lower viscosity

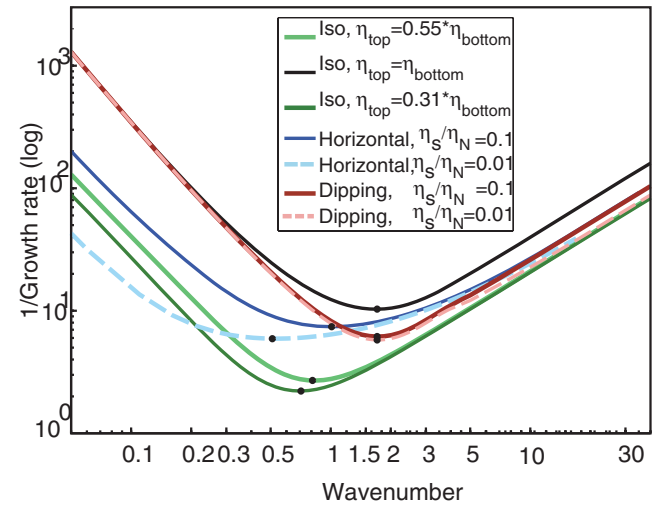


Figure 1. Growth-rate curves, plotting the growth rate of Rayleigh–Taylor instabilities versus the perturbation wavenumber, for models with varying degrees and orientations of anisotropy of a dense upper layer overlying an isotropic half-space: black— isotropic upper layer with viscosity equal to the viscosity of the bottom half-space; green curves— isotropic dense layer with viscosity equal to the average of the normal and shear viscosities of the anisotropic cases (dark green—geometric average, light green—arithmetic average); blue curves—horizontal easy shear direction (dark blue— $\eta_S/\eta_N = 0.1$, dashed light blue— $\eta_S/\eta_N = 0.01$); red curves—easy shear direction dipping at 45° (maroon— $\eta_S/\eta_N = 0.1$, dashed pink— $\eta_S/\eta_N = 0.01$). For the anisotropic cases, $\eta_N = \eta_{\text{bottom}}$. The minimum point of each curve, indicating the most unstable wavenumber for each configuration, is also shown.

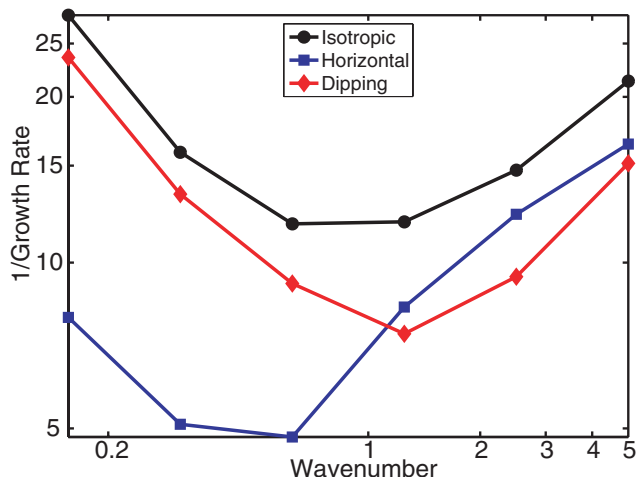


Figure 2. Growth-rate curves, plotting the non-dimensional growth rate versus perturbation wavenumber, for numerical experiments in which the anisotropic dense layer initially has a horizontal easy shear direction (blue line), a dipping easy shear direction (red line), or is isotropic (black line). The thickness of the dense layer is 0.15 of the box depth.

(green curves in Fig. 1). Also, the shape of the curve is changed compared to the isotropic case, and becomes flatter. For a dipping fabric (Fig. 1, red curves), the change is minor—the most unstable wavelength is equal to the isotropic and isoviscous one, and for long wavelengths the stability curves are almost identical for all degrees of anisotropy.

Fig. 2 shows the results from our numerical experiments. We plot the growth rate versus the wavenumber of the density perturbation for each initial configuration of the dense anisotropic layer: horizontal fabric (blue line, squares), 45°-dipping fabric (red line, diamonds) and isotropic (black line, circles). The results agree with the predictions from the analytical solution presented above—the fastest growth rate for the horizontal fabric is at a longer wavelength than that for the dipping fabric or for an isotropic layer, and the curve is indeed flatter at longer wavelengths. The minimum growth rate for a dipping fabric is at almost the same wavelength as that for an isotropic material, again in agreement with the analytical predictions. Fig. 3 shows the material distribution in the different model configurations after the fastest drips have sunk half of the box depth, as well as the approximate location of the initial perturbed interface (yellow curve). These snapshots demonstrate clearly that

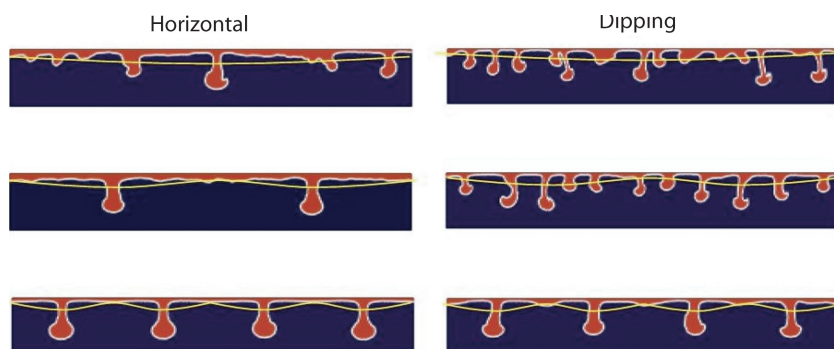


Figure 3. Material distribution for models with horizontal (left-hand panels) and dipping (right-hand panels) initial fabric of the dense top layer and various initial interface deflection wavelengths, taken after the fastest downwellings sink past half the box depth. Colour denotes the materials—blue is the isotropic buoyant material and red is the anisotropic denser material. The yellow curves show the approximate location of the initial density interface, exaggerated vertically for visual clarity.

the wavelength of the instabilities developing in the initially horizontal models is greater than of those developing in the initially dipping models. This emphasizes the advantage gained by using numerical experiments—the analytical solution gives insight into the behaviour of instabilities at small amplitudes, while the numerical experiments are essential for predicting the behaviour as the flow progresses and instabilities of finite-amplitude develop.

3 LATERALLY VARYING ANISOTROPY

Intrigued by the dramatic results for a simple model of a homogeneous anisotropic dense layer described above, we proceed and use numerical experiments to examine the effect of including lateral variations in the initial anisotropic fabric of the dense layer.

3.1 Model setup

Fig. 4 depicts the model geometry and initial and boundary conditions. The model domain is again a rectangular box with an aspect ratio of 1:6.4. The location and amplitude of the interface between the layers is the same as in Section 2. Following the findings of Section 2, we perturb the interface with a wavelength long enough to allow deformation at a wide range of wavelengths to develop freely. The dense layer now contains two anisotropic regions in the centre, each 1.6 wide, and two isotropic regions of the same high density near the edges. The anisotropic regions differ only by their initial fabric orientation—one (shown in red) initially has a horizontal easy shear direction, and the other has an easy shear direction initially dipping at 45° (shown in yellow). The viscosity of the buoyant layer is equal to the normal viscosity of the anisotropic layer. The shear viscosity of the anisotropic material is a factor of 10 less than its normal viscosity. We shift the anisotropic regions laterally in different models in order to change the phase between the viscosity structure and the density interface perturbation. We then examine the development of drips for each configuration.

3.2 Results—a heterogeneous upper layer

In Fig. 5, we show the instabilities that develop in our models. The different panels depict models with different configurations of the initial fabric domains, shown in red and yellow, as well as the results for an isotropic model for comparison (Fig. 5a). We also show the trace of the original density interface between the dense lithosphere

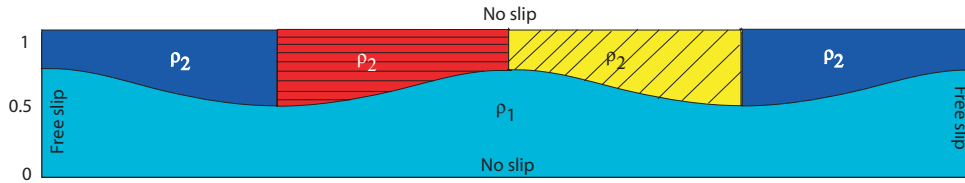


Figure 4. A schematic description of the model geometry and initial conditions. The colours denote the densities and rheologies: blue—*isotropic*, $\rho = 1$, $\eta_{\text{iso}} = 1$, red—*anisotropic with horizontal fabric*, $\rho = 1$, $\delta = 0.1$, yellow—*anisotropic with dipping fabric*, $\rho = 1$, $\delta = 10$, cyan—*isotropic*, $\rho = 0$, $\eta_{\text{iso}} = 1$). There is no slip on the top and bottom boundaries, and free slip is allowed along the side walls. The thickness of the top layer and the amplitude of the interface perturbation were exaggerated for clarity.

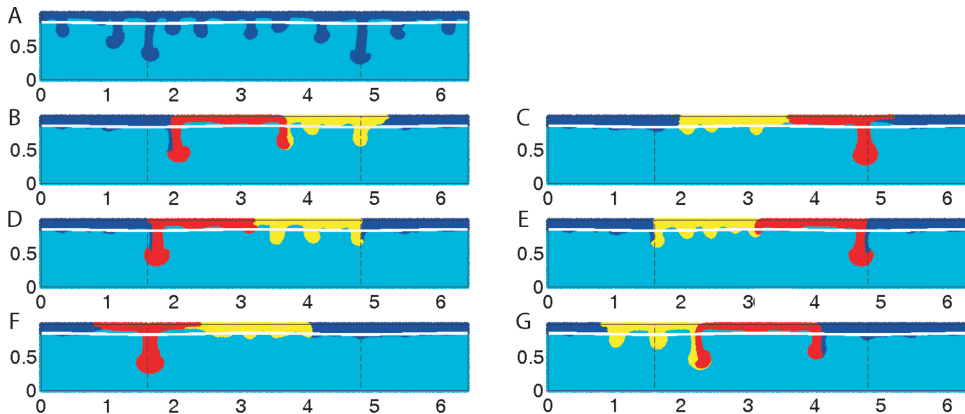


Figure 5. Material distribution in models with different configurations of initial anisotropic fabric taken after the fastest downwelling sinks over half the box depth. Panel A shows the results for an isotropic model. The black cosine curve at a depth of 0.15 marks the original interface between the dense and buoyant layers. The vertical dashed black lines show the deepest points of the original density interface, where the dense layer was thickest. Red material starts with a horizontal fabric; yellow material starts with a fabric dipping at 45° . Blue materials are isotropic. Interestingly both panels (b) and (g), which start with distinctly different material arrangements, show large downwellings comprised of both anisotropic materials, while others do not.

and the underlying mantle (black horizontal curve) and the location of the deepest points of the initial perturbation of the density interface (dashed vertical lines).

Several first-order observations can be made in Fig. 5. First, there is a striking difference between the instabilities that develop in the two anisotropic domains. Most notably, the wavelengths of the downwellings that develop in the domain with easy horizontal shear are much longer than the wavelengths in the dipping-fabric domains or in the isotropic model (Fig. 5a). In addition, the domain which starts with easy horizontal shear (red) develops instabilities faster than the domain which starts with easy shear direction dipping at 45° (yellow). Next, for several situations, the fastest-growing downwelling does not coincide with the locations of maximum thickness of the dense layer, but is offset horizontally by up to 0.5 of the box depth (Figs 5b and g). Finally, almost all of the fastest-growing instabilities occur near the edges of the domain of horizontal easy shear (excluding the case where the thickest part of the dense layer was exactly in the centre of the domain of initial horizontal anisotropy), but the instabilities that develop in the dipping easy shear domain develop in its interior. Evidently, the initial fabric and its lateral variations influence the flow significantly.

4 DISCUSSION

Our models are set up in a non-dimensional manner, for generality. It is interesting, though, to rescale the results to lithospheric dimensions. The dense layer (top 15 per cent of the box) corresponds to the viscously mobile part of the lithosphere, which is approximately its lowest 40 km. The viscosity of the lithosphere is temperature-

dependent, and is believed to decrease exponentially with depth, with a reasonable decay length of about 10 km (Molnar *et al.* 1998). If we take the viscosity at the base of the lithosphere to be 10^{19} Pa s (Hager 1991), then the average viscosity for a 40 km thick layer, calculated as $\langle \eta \rangle = \exp(\frac{\log \eta_1 + \log \eta_2}{2})$, is 7.4×10^{19} Pa s. Using the thickness of the lower lithosphere as the characteristic length scale, we can estimate the spacing between the isotropic instabilities as 130 km, and the wavelength of the longest anisotropic instabilities is close to 400 km. The lateral offset between the downwellings and the locations of maximum lithospheric thickness scales to a maximum of approximately 150 km. We rescale velocities based on the viscosity and density contrast, using the ‘Stokes Velocity’ ($V_{\text{Stokes}} = \frac{\Delta \rho * g * h^2}{\eta}$, where η is the effective viscosity of the dense layer, $\Delta \rho$ is the density contrast and h is the dense layer thickness). We estimate the difference between the density of the lower lithosphere and the density of the underlying asthenosphere as 40 kg m^{-3} (Molnar *et al.* 1998). After substituting the above values we can now calculate the scaling of time. We estimate that the time it takes for the drips to sink to a depth of 160 km (the stage shown in Fig. 5) is approximately 12 Myr. This duration is within the range of times estimated by Houseman & Molnar (1997) for removal of the base of an unstable thickened lithosphere. This time and distance of sinking imply an average sinking velocity of 14 mm yr^{-1} .

The models we present here are a preliminary attempt at this problem, and thus have some shortcomings when compared with the lithosphere. First, the fabric development rule we use is a simple rotational evolution law, and does not take into account factors such as temperature, strain rate, and recrystallization, all known to affect the development of CPO in rocks. Second, the rheology we use is a

Newtonian creep law, while in fact anisotropy due to CPO requires deformation in the dislocation creep regime, which is a power-law creep process. Additionally, all our experiments are carried out in two dimensions. There may be interesting consequences when these effects are studied in a 3-D setup, especially given the 3-D nature of some observed mantle instabilities (e.g. Yang & Forsyth 2006). A 3-D model would also be able to include orthorhombic symmetry and would not be constrained to the use of TI. Hopefully future work would be able to assess the significance of these factors and their implications.

Both our analytical solution and the numerical flow models predict that the wavelength of Rayleigh–Taylor instabilities would be longer for an anisotropic material, most significantly for a fabric favouring horizontal flow. Some intuitive understanding of this can be gained if we imagine a horizontally layered medium—it is much easier for such a medium to flow sideways by simple shear, and not to develop vertical drips. Drips will eventually develop in locations where the horizontal flow encounters resistance—for instance, in the form of a domain with a different fabric. This is likely the reason that the largest downwellings developed in the edges of the domains with initial horizontal easy shear direction (red domains in Fig. 5). If, on the other hand, the initial fabric is at an angle to the main acting force, it will be easier for the instabilities to thicken by pure shear and ‘break’ the layering structure, and hence will be more likely to follow a wavelength closer to the isotropic one. This result is in agreement with the experiments of Richter & Daly (1978), who found that anisotropy leads, in general, to longer wavelengths of instabilities. Saito & Abe (1984) performed a marginal stability analysis for a related model setup (bottom-heated Rayleigh–Bénard convection with stress free boundaries and horizontal layering) and, similarly to our results, found that the stability curves flatten out and that the minimum shifts to a longer wavelength with lower viscosity ratio.

We emphasize at this point that numerical techniques such as the one we use here have several important advantages. Analytical solutions, while elegant, give insight into the behaviour of instabilities only at small amplitudes, and thus numerical experiments are essential for predicting the flow as it progresses and instabilities of finite-amplitude develop. Additionally, the numerical technique we use is capable of modeling flows in which the fabric is evolving and the orientation of the anisotropy is not fixed in space, as opposed to the situation in our, as well as earlier (e.g. Richter & Daly 1978; Honda 1986), analytical solutions. It is also straightforward to include lateral variations of the anisotropy, a scenario highly relevant to tectonic processes in natural environments.

The strong effect of pre-existing fabric on the development of Rayleigh–Taylor instabilities may have important implications for the stability of the lithosphere. In our models, the fastest growing downwelling sometimes develops away from the initially deepest region of the density interface, due to the interaction between domains with different fabric orientation. This change in geometry may provide a simple explanation for the offset of the mantle drip beneath the Sierras (e.g. Saleeby & Forster 2004). Our findings of the effect of AV on the wavelength of instabilities should also be considered in the context of other locations, for example Tibet. Conrad & Molnar (1997) argued that the wavelength of Rayleigh–Taylor instabilities predicted to arise from the collision between India and Eurasia is much shorter than the wavelength of the Tibetan plateau, and hence such instabilities are unlikely to be the cause of the rapid uplift of the plateau at 5–10 Myr ago. If, however, the existing fabric in the collision zone was such that it leads to longer wavelengths, this possibility may need to be reconsidered.

The points of contact between regions with different existing fabric appear to have unique significance. This hints that when tectonic units which have gone through a different evolution and developed different fabrics are juxtaposed, this contact point may be particularly unstable. An example of such a situation may be the placing of a spreading centre, which is characterized by horizontal easy-shear planes, next to a region that is more horizontally resistant. When this combination is put under compression, the horizontal easy shear planes will be unstable at the contact point, which may lead to initiation of downwelling and perhaps even subduction. Subduction initiation at extinct spreading centres is likely the explanation for the subduction zone at the Macquarie region south of New Zealand (Lebrun *et al.* 2003) and near the Oman ophiolite (Michibayashi & Mainprice 2004). Our results clearly show that additional knowledge of the anisotropic fabric of the lithosphere, and, specifically, the orientation of dipping fabrics, can shed light on different tectonic problems, and highlights the importance of overcoming the difficulties in making such measurements (e.g. Chevrot & van der Hilst 2003).

5 SUMMARY

We show the dramatic effect of AV on the development of Rayleigh–Taylor instabilities. The wavelength, timing and shape of the instabilities that develop in our models are strongly affected by the initial fabric prescribed. The most notable effect of AV on Rayleigh–Taylor instabilities, demonstrated here both analytically and numerically, is the shift to longer wavelengths when the initial fabric of the dense material favours horizontal flow (horizontal or vertical fabric). The interplay between regions with different orientations of initial fabric gives rise to a variety of features, such as an offset of the main downwellings away from the deepest point of the perturbed interface, and demonstrates the importance of considering the deformation history of all the units participating in a tectonic setting. Our results show that for the study of lithospheric instabilities, and likely of other mantle processes, the common isotropic approximation may not be accurate, and hence AV should be included.

ACKNOWLEDGMENTS

We are grateful for helpful discussions with Linda Elkins-Tanton, Ming Fang, Greg Hirth, Eduard Kaminski, Laurent Pouilloux and Andrea Tommasi. A thoughtful review by Gregory Houseman helped greatly to improve the manuscript. The research presented here was supported by NSF under grants EAR-0337697 and EAR-0409564.

REFERENCES

- Bai, Q. & Kohlstedt, D.L., 1992. High-temperature creep of olivine single crystals. II: Dislocation structures, *Tectonophysics*, **206**(1–2), 1–29.
- Belytschko, T., Liu, W.K. & Moran, B., 2001. *Non-linear Finite Elements for Continua and Structures*, John Wiley and Sons, Chichester, UK.
- Billen, M.I. & Houseman, G.A., 2004. Lithospheric instability in obliquely convergent margins: San Gabriel Mountains, southern California, *J. geophys. Res.*, **109**, B01404.
- Chevrot, S. & van der Hilst, R.D., 2003. On the effects of a dipping axis of symmetry on shear wave splitting measurements in a transversely isotropic medium, *Geophys. J. Int.*, **152**, 497–505.
- Christensen, U., 1987. Some geodynamical effects of anisotropic viscosity, *Geophys. J. R. astr. Soc.*, **91**, 711–736.
- Conrad, C.P. & Molnar, P., 1997. The growth of Rayleigh–Taylor-type instabilities in the lithosphere for various rheological and density structures, *Geophys. J. Int.*, **129**, 95–112.

- Conrad, C.P. & Molnar, P., 1999. Convective instability of a boundary layer with temperature- and strain-rate-dependent viscosity in terms of 'available buoyancy', *Geophys. J. Int.*, **139**, 51–68.
- Crampin, S., 1978. Seismic-waves propagating through a cracked solid: polarization as a possible dilatancy diagnostic, *Geophys. J. R. astr. Soc.*, **53**, 467–496.
- Durham, W.B. & Goetze, C., 1977. Plastic flow of oriented single crystals of olivine 1. Mechanical data, *J. geophys. Res.*, **82**, 5737–5754.
- Elkins-Tanton, L.T. & Hager, B.H., 2000. Melt intrusion as a trigger for lithospheric foundering and the eruption of the Siberian flood basalts, *Geophys. Res. Lett.*, **27**, 3937–3940.
- England, P. & Houseman, G., 1989. Extension during continental convergence, with application to the Tibetan Plateau, *J. geophys. Res.*, **94**, 17 561–17 579.
- Fan, W.M., Zhang, H.F., Baker, J., Jarvis, K.E., Mason, P.R. & A., M., 2000. On and off the North China Craton; where is the Archaean keel? In commemoration of Keith Gordon Cox, 1933–1998, *J. Petrol.*, **41**, 933–950.
- Hager, B.H., 1991. Mantle viscosity—a comparison of models from post-glacial rebound and from the geoid, plate driving forces, and advected heat flux, in *Glacial Isostasy, Sea Level and Mantle Rheology*, p. 21, eds Sabadini, R., Lambeck, K. & Boscini, E., Kluwer Academic Publishers, Dordrecht, Netherlands.
- Hager, B.H. & O'Connell, R.J., 1981. A simple global model of plate dynamics and mantle convection, *J. geophys. Res.*, **86**, 4843–4867.
- Holtzman, B.K., Kohlstedt, D.L., Zimmerman, M.E., Heidelbach, F., Hiraga, T. & Hustoft, J., 2003. Melt segregation and strain partitioning: implications for seismic anisotropy and mantle flow, *Science*, **301**, 1227–1230.
- Honda, S., 1986. Strong anisotropic flow in a finely layered asthenosphere, *Geophys. Res. Lett.*, **13**, 1454–1457.
- Houseman, G.A. & Molnar, P., 1997. Gravitational Rayleigh–Taylor instability of a layer with nonlinear viscosity and convective thinning of continental lithosphere, *Geophys. J. Int.*, **128**, 125–150.
- Houseman, G.A., McKenzie, D.P. & Molnar, P., 1981. Convective instability of a thickened boundary layer and its relevance for the thermal evolution of continental convergent belts, *J. geophys. Res.*, **86**, 6115–6132.
- Humphreys, E.D. & Clayton, R.W., 1990. Tomographic image of the Southern California mantle, *J. geophys. Res.*, **95**, 19 725–19 746.
- Humphreys, E.D. & Hager, B.H., 1990. A kinematic model for the late Cenozoic development of southern California crust and upper mantle, *J. geophys. Res.*, **95**, 19 747–19 762.
- Kaminski, É. & Ribe, N.M., 2001. A kinematic model for recrystallization and texture development in olivine polycrystals, *Earth planet. Sci. Lett.*, **189**, 253–267.
- Karato, S., Zhang, S., Zimmerman, M.E., Daines, M.J. & Kohlstedt, D.L., 1998. Experimental studies of shear deformation of mantle materials: towards structural geology of the mantle, *Pure appl. Geophys.*, **151**, 589–603.
- Kay, S.M., Coira, B. & Viramonte, J., 1994. Young mafic back arc volcanic rocks as indicators of continental lithospheric delamination beneath the Argentine Puna plateau, central Andes, *J. geophys. Res.*, **99**, 24 323–24 339.
- Kohler, M.D., 1999. Lithospheric deformation beneath the San Gabriel Mountains in the southern California Transverse Ranges, *J. geophys. Res.*, **104**, 15 025–15 042.
- Lebrun, J.-F., Lamarche, G. & Collot, J.-Y., 2003. Subduction initiation at a strike-slip plate boundary: the Cenozoic Pacific–Australian plate boundary, south of New Zealand, *J. geophys. Res. (Solid Earth)*, **108**.
- Mandal, N., Chakraborty, C. & Samanta, S.K., 2000. An analysis of anisotropy of rocks containing shape fabric of rigid inclusions, *J. Struct. Geol.*, **22**, 831–839.
- Maupin, V., Garnero, E.J., Lay, T. & Fouch, M.J., 2005. Azimuthal anisotropy in the D' layer beneath the Caribbean, *J. geophys. Res.*, **110**(B9), B08301.
- Michibayashi, K. & Mainprice, D., 2004. The role of pre-existing mechanical anisotropy on shear zone development within oceanic mantle lithosphere: an example from the Oman ophiolite, *J. Petrol.*, **45**(2), 405–414.
- Molnar, P., Houseman, G.A. & Conrad, C.P., 1998. Rayleigh–Taylor instability and convective thinning of mechanically thickened lithosphere: effects of non-linear viscosity decreasing exponentially with depth and of horizontal shortening of the layer, *Geophys. J. Int.*, **133**, 568–584.
- Moresi, L., Dufour, F. & Mühlhaus, H.-B., 2002. Mantle convection modeling with viscoelastic/brittle lithosphere: numerical methodology and plate tectonic modeling, *Pure appl. Geophys.*, **159**, 2335–2356.
- Moresi, L., Dufour, F. & Mühlhaus, H.-B., 2003. A Lagrangian integration point finite element method for large deformation modeling of viscoelastic geomaterials, *J. Comput. Phys.*, **184**, 476–497.
- Mühlhaus, H.-B., Moresi, L., Hobbs, B. & Dufour, F., 2002. Large amplitude folding in finely layered viscoelastic rock structures, *Pure appl. Geophys.*, **159**, 2311–2333.
- Mühlhaus, H.-B., Moresi, L. & Cada, M., 2004. Emergent anisotropy and flow alignment in viscous rock, *Pure appl. Geophys.*, **161**, 2451–2463.
- Murphy, J.B., van Staal, C.R. & Keppie, J.D., 1999. Middle to late Paleozoic Acadian Orogeny in the northern Appalachians: a Laramide-style plumemodified orogeny?, *Geology*, **27**, 653–656.
- Pouilloux, L., Kaminski, E. & Labrosse, S., 2007. Anisotropic rheology of a cubic medium and the implications for geologic materials, *Geophys. J. Int.*, **170**, 876–885.
- Richter, F.M. & Daly, S.F., 1978. Convection models having a multiplicity of large horizontal scales, *J. geophys. Res.*, **83**, 4951–4956.
- Robinson, P., 1993. Acadian magmatism and metamorphism in New England: a product of mantle/lithosphere delamination in front of an east-dipping subduction zone? *Geol. Soc. Am. Abstr. Prog.*, **25**(6), Abs. 179.
- Saito, M. & Abe, Y., 1984. Consequences of anisotropic viscosity in the Earth's mantle (in Japanese, with English Abstract), *Zisin*, **37**, 237–245.
- Saleeby, J. & Forster, Z., 2004. Topographic response to mantle lithosphere removal in the southern Sierra Nevada region, California, *Geology*, **32**, 245–248.
- Schubert, G., Turcotte, D.L. & Olson, P., 2001. *Mantle Convection in the Earth and Planets*, pp. 956, ISBN 052135367X, Cambridge University Press, Cambridge, UK.
- Treagus, S.H., 2003. Viscous anisotropy of two-phase composites, and applications to rocks and structures, *Tectonophysics*, **372**, 121–133.
- Vauchez, A., Tomassi, A. & Barroul, G., 1998. Rheological heterogeneity, mechanical anisotropy and deformation of the continental lithosphere, *Tectonophysics*, **296**, 61–86.
- Weijermars, R., 1992. Progressive deformation in anisotropic rocks, *J. Struct. Geol.*, pp. 723–742.
- Wendt, A.S., Mainprice, D., Rutter, E. & Wirth, R., 1998. A joint study of experimental deformation and experimentally induced microstructures of pretexured peridotites, *J. geophys. Res.*, **103**, 18 205–18 222.
- Wenzel, T., Mertz, D.F., Oberhänsli, R., Becker, T. & Renne, P.R., 1997. Age, geodynamic setting, and mantle enrichment processes of a K-rich intrusion from the Meissen massif (northern Bohemian massif) and implications for related occurrences from the mid-European Hercynian, *Int. J. Earth Sci.*, **86**, 556–570.
- Whitehead, J.A., 1986. Buoyancy-driven instabilities of low-viscosity zones as models of magma-rich zones, *J. geophys. Res.*, **91**, 9303–9314.
- Wu, F.-Y., Lin, J.-Q., Wilde, S.A., Zhang, X. & Yang, J.-H., 2005. Nature and significance of the Early Cretaceous giant igneous event in eastern China, *Earth planet. Sci. Lett.*, **233**, 103–119.
- Yang, Y. & Forsyth, D.W., 2006. Rayleigh wave phase velocities, small-scale convection, and azimuthal anisotropy beneath southern California, *J. geophys. Res. (Solid Earth)*, **111**(B10), B07306.
- Zhang, Z. & Karato, S.I., 1995. Lattice preferred orientation in olivine aggregates deformed in simple shear, *Nature*, **375**, 774–777.

APPENDIX A: DERIVATION OF ANALYTICAL SOLUTION

We begin by defining the following anisotropic constitutive relations, which describe a transversely isotropic (TI) material in the two special cases considered here of (1) easy-shear on horizontal/vertical planes and (2) easy-shear on planes dipping at 45°:

$$\sigma_{xx} = 2\eta_{ps}\dot{\epsilon}_{xx} \quad (\text{A1a})$$

$$\sigma_{zz} = 2\eta_{ps}\dot{\epsilon}_{zz} \quad (\text{A1b})$$

$$\sigma_{xz} = \eta_{ss}\dot{\epsilon}_{xz}, \quad (\text{A1c})$$

where η_{ps} is a viscosity corresponding to pure shear stresses, and η_{ss} corresponding to simple-shear. For a material with a horizontal easy-shear direction (horizontal layering, for instance) η_{ss} is equivalent to η_S defined in Section 2.1, $\eta_{ps} \equiv \eta_N$, and $\eta_{ss} < \eta_{ps}$. For an anisotropic material with a dipping easy-shear direction, $\eta_S \equiv \eta_{ps} < \eta_{ss} \equiv \eta_N$. For an isotropic material, $\eta_{ps} = \eta_{ss}$. This constitutive relation can be derived from a matrix form similar to that in eq. (4): $\sigma_{ij} = 2\eta_N \epsilon_{ij} - 2(\eta_N - \eta_S)\Lambda_{ijkl} \epsilon_{kl}$, where Λ is an alignment tensor reflecting the orientation of the symmetry axis. Then, the transformation from a horizontal symmetry anisotropy to a dipping symmetry can be achieved by a rotation of the 4th-order tensor Λ .

In our analytical solution, we employ the propagator matrix technique (e.g. Hager & O'Connell 1981) to calculate the growth rate of Rayleigh–Taylor instabilities as a function of the wavelength of the density perturbation between the two materials. We set $z = 0$ at the interface between the layers, $z = 1$ at the top of the dense layer, and the initial location of the density interface as $w = w_0 \cos(kx)$. For the horizontal and 45°-dipping orientations we consider here, this definition of the interface perturbation leads to $v_x, \sigma_{zz} \propto \cos(kx)$, and $v_z, \sigma_{xz} \propto \sin(kx)$, where k is the wavenumber. For other orientations there may be a phase shift with depth (Christensen 1987). Thanks to the orthogonality of the trigonometric basis functions, we can write a simplified set of equations for each wavenumber. We define a vector $\mathbf{u} = [v, u, \sigma_{zz}, \sigma_{xz}]$, where v is the vertical velocity, u is the horizontal velocity, σ_{zz} is the normal stress in the z direction, σ_{xz} is the shear stress, and x and z are the horizontal and vertical coordinates. After some manipulation, this definition of \mathbf{u} enables us to express the equations of flow in each layer for every k as

$$D\mathbf{u} = \mathbf{A}\mathbf{u} + \mathbf{b}, \quad (\text{A2})$$

where $D = \frac{\partial}{\partial z}$, and \mathbf{b} is a forcing term. The matrix \mathbf{A} is where the AV is manifested.

The definition of the anisotropic constitutive relation above leads to a matrix \mathbf{A} of the form:

$$\mathbf{A} = \begin{bmatrix} 0 & -k & 0 & 0 \\ k & 0 & 0 & \eta_{ss}^{-1} \\ 0 & 0 & 0 & -k \\ 0 & 4\eta_{ps}k^2 & k & 0 \end{bmatrix}. \quad (\text{A3})$$

When $\eta_{ps} = \eta_{ss}$ (isotropic material), the expression in (A3) is equal to the matrix \mathbf{A} given by Hager & O'Connell (1981). Otherwise, it reflects the AV of the material by including the two different viscosities.

The solution to eq. (A2) is of the form

$$\mathbf{u}(z) = e^{\mathbf{A}(z-z_0)}\mathbf{u}(z_0) + \int_{z_0}^z e^{\mathbf{A}(z-\xi)}\mathbf{b}(\xi)d\xi. \quad (\text{A4})$$

We define the propagator matrix $\mathbf{P}(z, z_0) = e^{\mathbf{A}(z-z_0)}$, so that the velocities and stresses can be expressed as

$$\mathbf{u}(z) = P(z, z_0)\mathbf{u}(z_0) + \sum_{i=1}^n P(z, \xi_i)\mathbf{b}(\xi_i)\Delta\xi_i, \quad (\text{A5})$$

where ξ_i is the depth at the centre of a the i th layer and $\Delta\xi_i$ is the layer thickness. The propagator matrix for an anisotropic material will naturally be different than the propagator matrix for an isotropic material, given the difference in the corresponding \mathbf{A} matrices. The boundary conditions for our problem are no-slip at the top boundary

($z = 1$), which we take to be the base of the rigid part of the lithosphere, and vanishing of the velocities and stresses as $z \rightarrow -\infty$. We can express the boundary conditions using the vector \mathbf{u} defined earlier:

$$\mathbf{u}(z = 1) = [0, 0, \sigma_{zz}^t, \sigma_{xz}^t], \quad \mathbf{u}(z = -\infty) = [0, 0, 0, 0]. \quad (\text{A6})$$

In order to fulfill the boundary condition as $z \rightarrow -\infty$, \mathbf{u} just below the interface has to be of the form $\mathbf{u}(z = 0^-) = [C_1/2k, C_2/2k, C_1, C_2]$, where C_1, C_2 are the σ_{zz} and σ_{xz} at the interface. We add a normalized forcing term which here represents the gravitational forcing in the z direction. Thus \mathbf{u} across the interface, at the bottom of the dense layer, becomes $\mathbf{u}(z = 0^+) = [C_1/2k, C_2/2k, C_1 + 1, C_2]$. We propagate this $\mathbf{u}(z = 0^+)$ upwards to the top interface using the anisotropic propagator matrix P_{ani} : $\mathbf{u}(z = 1) = P_{\text{ani}}\mathbf{u}(z = 0^+)$. From the no-slip boundary condition at the top, the first two components of the resulting vector are equal to zero. We now have two equations and two unknowns— C_1 and C_2 . We solve for these two unknowns and use the result to calculate the vertical velocity at the interface.

The change in the interface location with time is equal to the vertical velocity at the interface— $v(z = 0)$, where v is the vertical velocity. A result of the derivation described above is that the vertical velocity at the interface is proportional to the perturbation of the interface, that is:

$$v(z = 0) \equiv \frac{\partial w}{\partial t} \propto w. \quad (\text{A7})$$

Therefore, the change in the interface depth follows an exponential growth rule: $w(z, t) = e^{\frac{t}{\tau}}$, which gives the dependence of the growth rate τ on the model parameters:

$$\tau = \frac{1}{K(\eta_{ps}, \eta_{ss}, k)}, \quad (\text{A8})$$

K is a complicated function of the viscosities and the wavenumber, of the form:

$\Delta\rho g \times [a \text{ sum of exponents of powers of } \eta_N, \eta_{ss}, \text{ and } k]$. The exact expression is too long to give here explicitly, but can be obtained using the Matlab code in the Supplementary Material (Appendix S1). The resulting relationship between $1/K$ (τ) for a range of wavenumbers and a set of viscosity ratios is demonstrated in Fig. 1; Fig. S1 (Supplementary Material) shows a similar calculation for a range of viscosity ratios and $k = 0.1$.

A careful inspection of the anisotropic matrix A_{ani} and the anisotropic propagator matrix P_{ani} reveals a very interesting phenomenon—an oscillatory behaviour with depth for certain viscosity ratios. Let us define δ , the viscosity ratio, as $\delta = \frac{\eta_{ss}}{\eta_{ps}}$. As we noted earlier, for a material with a horizontal easy-shear direction $\eta_{ss} < \eta_{ps}$, and thus $\delta < 1$, while for a material with a dipping easy-shear direction $\eta_{ss} > \eta_{ps}$ and $\delta > 1$. The eigenvalues of the matrix \mathbf{A} are used in the expression for the propagator matrix and control the behaviour of the velocities and stresses in the medium. For an isotropic material, these eigenvalues are real and repeated, and the propagator matrix includes additional terms depending linearly on the depth— $P \propto (1 \pm kz)e^{\pm kz}$ (Hager & O'Connell 1981). The anisotropic \mathbf{A} matrix has, on the other hand, four distinct eigenvalues, of the form:

$$\lambda_i = \pm k \left(\frac{2 - \delta \pm 2\sqrt{1 - \delta}}{\delta} \right)^{\frac{1}{2}}. \quad (\text{A9})$$

All the eigenvalues for a material with horizontal fabric ($\delta < 1$) are real, leading to a propagator matrix (and thus velocities and

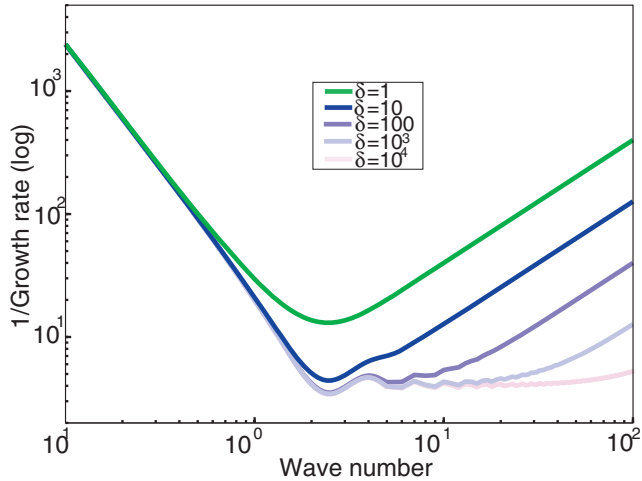


Figure A1. Growth-rate curves, plotting the growth rate of Rayleigh–Taylor instabilities versus the perturbation wavenumber, for models of an anisotropic dense upper layer overlaying an anisotropic half-space, both with a dipping easy-shear direction. The colours denote different degrees of anisotropy: green—isotropic materials; blue to pink—increasing degrees of viscosity contrast between the shear and normal viscosities. The oscillatory behaviour, characteristic of materials with dipping easy-shear directions, is apparent. As the viscosity contrast increases, the curves flatten for short wavelength.

stresses) that are proportional to $e^{\pm\lambda_i z}$. Anisotropy with a 45° dipping easy-shear direction ($\delta > 1$) implies that the four eigenvalues are complex, and thus the velocities and stresses are proportional to $\cos(\text{Im}(\lambda_i)z)e^{\pm\text{Re}(\lambda_i)z}$ and $\sin(\text{Im}(\lambda_i)z)e^{\pm\text{Re}(\lambda_i)z}$. This gives rise to a non-monotonic behaviour of the velocity and stress fields with depth for dipping anisotropy, plotted in Fig. A1. This oscillatory behaviour is strongly enhanced when both the dense layer and the buoyant half-space underneath have an anisotropic, dipping fabric. The growth-rate curves for this case are given in Fig. A1; the non-monotonic fluctuations are obvious, especially as δ becomes larger.

SUPPLEMENTARY MATERIAL

The following supplementary material is available for this article:

Appendix S1. MATLAB code for the complicated function of the viscosities and the wavenumber (PDF file).

Figure S1. The resulting relationship between $1/K(\tau)$ for a range of wavenumbers and a set of viscosity ratios (PDF file).

This material is available as part of the online article from: <http://www.blackwell-synergy.com/doi/abs/10.1111/j.1365-246X.2008.03731.x>

(this link will take you to the article abstract).

Please note: Blackwell Publishing are not responsible for the content or functionality of any supplementary materials supplied by the authors. Any queries (other than missing material) should be directed to the corresponding author for the article.